Model-oriented ocean tomography using higher frequency, bottom-mounted hydrophones

James K. Lewis
Scientific Solutions, Inc., 4875 Kikala Road, Kalaheo, Hawaii 96741

Jason Rudzinsky
Applied Physical Sciences, Corp., 2 State Street, Suite 300, New London, Connecticut 06320

Subramaniam Rajan, Peter J. Stein, and Amy Vandiver
Scientific Solutions, Inc., 99 Perimeter Road, Nashua, New Hampshire 03063

The KauaiEx Group

A tomographic scheme is presented that ingests ocean acoustic measurements into an ocean model using data from bottom-mounted hydrophones. The short distances between source-receiver pairs (1–10 km) means arrival times at frequencies of 8–11 kHz are readily detectable and often distinguishable. The influence of ocean surface motion causes considerable variability in acoustic travel times. Techniques are presented for measuring travel times and removing the variability due to surface waves. An assimilation technique is investigated that uses differences in measured and modeled acoustic travel times to impose corrections on the oceanographic model. Equations relating travel time differences to oceanographic variables are derived, and techniques are presented for estimating the acoustic and ocean model error covariance matrices. One test case using a single source-receiver pair shows that the tomographic information can have an impact on constraining the solution of the ocean circulation model but can also introduce biases in the predictions. A second test case utilizes knowledge of a bias in a model-predicted variable to limit grid cells that are impacted by the tomographic data. In this case, using the tomographic data results in significant improvements in the model predictions without introducing any biases. © *2005 Acoustical Society of America.*
[DOI: 10.1121/1.1893355]

I. INTRODUCTION

Variations in the travel times of acoustic signals are known to be related to the spatial and temporal changes in water column temperatures, salinities, and currents. As such, acoustic tomography can provide relevant and important information on the characteristics of the water column.[1] Moreover, the travel time of an acoustic pulse from fixed and well-separated source and receiver locations may be considered a more robust measure of spatially averaged oceanographic variables (e.g., sound speed or temperature) than are point measurements.[2,3] This results from the fact that the acoustic parameter is an integral over space, while point measurements are susceptible to local, small-spatial scale noise.

In the work presented here, we develop a tomographic formulation that uses travel time measurements of relatively high frequency (~10 kHz) acoustic transmissions across fixed, omnidirectional, bottom-mounted acoustic transducers. Measured travel times along distinct ray paths are expressed as the difference between a reference travel time (through an environment with a reference sound speed structure) and a weighted sum of sound speed perturbations (with respect to the reference sound speed structure) in a gridded plane containing the source and receiver. To constrain the solution of the sound speed perturbation vector, a spatial covariance structure is imposed. Instead of directly inverting for the

sound speed perturbation (i.e., inverse tomography), we utilize a suboptimal assimilation process in which expressions relating the acoustic travel time measurements to ocean variables are used to ingest the acoustic data into a dynamic ocean model of the region. A spatial covariance matrix weights the acoustic observations and spatially distributes their influence throughout the ocean model domain. The assimilation scheme allows the acoustic observation to locally influence both nowcasts and forecasts of variables in the ocean model (e.g., water temperature). Our system is somewhat similar to that which would be implemented using a dynamic state space/parameter estimation scheme (e.g., a Kalman filtering approach[4]) except that dynamic updates to the covariance matrix are not performed with every new set of acoustic observations and model fields.

As a test bed for our tomographic studies, we have used two primary assets. The first is Pacific Missile Range Facility (PMRF) off the west coast of Kauai, Hawaii. PMRF has 15 bottom-mounted sources that operate in the 8–11-kHz band. PMRF has an additional 178 bottom-mounted receivers. These assets, used by PMRF primarily for localization, communications, and safety purposes, provide for the capability of transmitting and receiving acoustic data throughout the range. The distances between source-receiver pairs in the shallow regions of the range are relatively small (as short as 1 km). The arrival times in the 8–11-kHz band are readily detectable. Although the configuration of all hydrophones
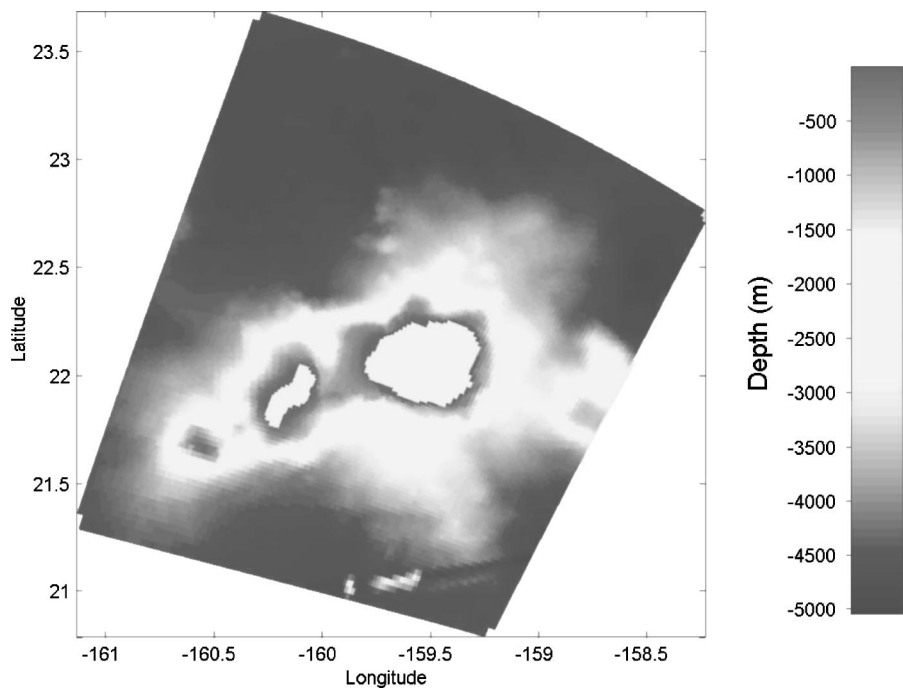
FIG. 1. Domain and depth field for the Kauai (island to the east) and Niihau (island toward the west) ocean model. PMRF reaches from between the islands northward to $\sim$23 °N.

being bottom-mounted is unconventional, such an arrangement has tomographic benefits in that there is effectively no positional uncertainty of the sensors. However, the acoustic signals of greatest use from bottom-mounted systems interact with the ocean surface and are, therefore, subject to the influence of surface waves. As a result, arrival times in the relatively high-frequency range of interest (8–11 kHz) can have considerable short-term variability due to the surface wave fields, often the dominate source of variability.

The second asset we employed is the ocean circulation model that encompasses the waters of PMRF off the west end of the island of Kauai (Fig. 1). The authors developed this model for the purposes of obtaining estimates of the spatial and temporal variations of oceanographic parameters that would impact sound speed structure. The hydrodynamic model is executed on a daily basis, predicting temperatures (T), salinities (S), and currents (U) at horizontal resolutions as high as 900 m and 28 levels in the vertical. The model provides a means of specifying realistic sound speed structure in space and time under varying tidal, atmospheric, and wave conditions. As such, the model offers a means of estimating acoustic ray arrival times in the ocean surrounding PMRF. In addition, the ocean model provides the testing capability of a method for assimilating acoustic travel times to impact model-calculated T, S, and U using a formulation that is an analog of the physical-space statistical analysis system (PSAS) data assimilation scheme.[5]

Using our model-oriented assimilation approach (directly relating acoustic data to the T, S, and U of a model) has some distinct benefits for providing more accurate model predictions. First, acoustic data reflect information about a volume within the water column and provide a natural means for obtaining spatially averaged measures of oceanographic variables. This is opposed to single point or vertical profile observations that are susceptible to small spatial-scale variations, noise, and uncertainties that may limit their utility as ocean model inputs. Second, the PSAS scheme allows even just one source-receiver pair to influence the model solutions in a large volume of water surrounding the path of the acoustic ray between the source and receiver. This is achieved utilizing estimates of the spatial error covariance matrices for the acoustic observations and the model variables.

Here we present formulations for quantifying the observed arrival times of acoustic rays whose paths have interacted with the ocean surface. Arrival time anomalies are determined relative to a monthly sound velocity structure based on the three-dimensional grid structure of the hydrodynamic model of the PMRF region. We present transforms for determining a model-related travel time anomaly along the path of the transmitted acoustic ray. It is shown that the differences between the model and observed travel time anomalies can be transformed back to adjustments of model-predicted water temperatures, salinities, and currents.

There are several elements involved with this work. These include collection and analysis of arrival times and arrival time anomalies for specific acoustic paths, the details of the numerical ocean model, and the specific construct of the PSAS to relate travel time anomalies to model-predicted variables for assimilation into the ocean model. Each element will be discussed as well as the details of test cases in which travel times from one source-receiver pair were assimilated into the ocean model.

II. THE OCEAN MODELS FOR PMRF

A hydrodynamic model, an adaptation of the Blumberg and Mellor model,[6] has been implemented for the waters surrounding Kauai and Niihau, Hawaii (Fig. 1). This particular version of the model uses a semi-implicit solution scheme for solving for the sea surface height field[7] and a hybrid z-level coordinate system in the vertical[8] to minimize problems that can arise with the original bottom-following sigma-

coordinate system when using steep bathymetry and realistic temperature and salinity profiles. The bathymetry (Fig. 1) is from the Smith-Sandwell topography[9] augmented with higher resolution sounding data obtained from NOAA and PMRF. A fundamental length scale that characterizes some of the flow-field activity in the region is the baroclinic radius of deformation, approximately 20 km. Therefore, the model grid spacing is set at 2–3 km around the open boundaries of the domains to approximately 1 km around the shoreline of Kauai. In addition, the total horizontal domain is well beyond 20 km off the islands.

Observed T-S characteristics were used in specifying the vertical resolution of the model. We chose the vertical grid structure (28 active levels) with higher resolution within the top 100 m and at those depths at which salinity extremes exist. This allows advective inflow conditions specified at the open boundaries to better maintain the observed T-S structure within the model domain.

We utilized the open boundary condition presented in Lewis *et al.*,[10] specifying the tidal sea level elevations and phases along the open boundaries of the model domains. The boundary values were obtained from the Oregon State University tidal model TPXO.3[11] but ''tuned'' to match observed amplitudes and phases for Kauai. The model was forced at the open boundaries with the M_2, S_2, N_2, O_1, K_1, and P_1 tidal constituents. The model error for the largest tidal constituent, the M_2 tide, is less than 4%, and the errors for the other constituents are similar or smaller in magnitude.

In addition to the ocean circulation, surface waves were modeled using Delft University of Technology's SWAN (simulating waves nearshore).[12,13] SWAN is a two-dimensional wave spectra model that can perform using a curvilinear-orthogonal grid. The two-dimensional spectra ability results in being able to realistically simulate the wide range of wave conditions typically encountered in the world's oceans. A curvilinear-orthogonal grid allows SWAN to use the same computational grid (and associated depths) as that used by the ocean circulation model. The means of allowing the interactions between currents and waves is greatly facilitated with the use of the same grids by both the wave and circulation models.

A. Initialization and forcing fields

In addition to tides, the model utilizes the Navy's daily modular ocean data assimilation system (MODAS) as a daily estimate of the three-dimensional T-S structure within the model domain. This is used to introduce the mesoscale circulation field into the model domain. MODAS fields use satellite sea surface temperatures, satellite altimetry, bathythermograph data, and results from other models to determine the T-S structure within a region. Our ocean model employs a scheme that nudges[14] the model-predicted temperatures and salinities to the MODAS temperatures and salinities. The nudging parameter T^* had a value of 0.75 days, representing a fairly strong nudge. However, tests showed that the model-predicted T and S often had substantial variations away from the MODAS T-S values as dictated by the governing physics within the model.

Atmospheric forcing from the National Centers for Environmental Prediction (NCEP) includes momentum, heat, and mass fluxes at the air-sea interface. With these, the ocean model can include wind forcing, precipitation minus evaporation, and sensible, evaporative, and radiative heat fluxes. The SWAN model is forced by the NCEP surface wind velocity and wave fields that are generated far from Hawaii and then propagate to the islands. To account for this latter factor, SWAN ingests NOAA's WaveWatchIII wave spectra information along the open boundaries of the model domain.

Since waves can have a significant impact on ocean circulation,[15] the ocean circulation model utilized the surface wave model results to calculate (1) wave-enhanced bottom friction, (2) Stokes drift and the Coriolis wave stress, (3) radiation stresses, (4) wave-related mixing length at the ocean surface, and (5) the virtual tangential surface stress.

B. Model accuracy

As a measure of the accuracy of the ocean circulation model, predictions and corresponding observations of water temperature were used to calculate an rms model error as a function of depth. During June and July 2003, 175 bathythermographs (BTs) were collected. Model temperatures were interpolated in space and time to these BT data to calculate the rms error for T. Values of rms errors range from $\Delta T = 0.22\,°C$ to $0.96\,°C$, which translates to sound speed errors of 1.2–4.8 m/s, assuming $\partial c / \partial T \approx 4.947$ m/s/°C, where c is sound speed. Since salinity does vary significantly with depth in the Hawaii region, errors in predicting water temperature will be the primary cause of errors in sound speed in the water column.

III. CONSTRUCTS RELATED TO THE PSAS DATA ASSIMILATION

Some of the forcing fields contain observations, such as the MODAS fields and the initial conditions of the atmospheric fields. But there is very little water column data represented within the forcing data, especially for forcing fields representing future conditions. Acoustic travel time information represents *in situ* data that could be assimilated into the ocean model to constrain the solutions of the model, and hopefully increase the accuracy of the model.

A. Simulating acoustic paths and travel times

The ocean model T-S structure can be used to calculate sound speed profiles (SSP) using expressions relating T, S, and depth to sound speed. This was done to obtain SSPs at a vertical resolution of 5 m and a horizontal resolution of 150 m. Knowing the precise locations of the PMRF sources and receivers, we used the SSP in the Bellhop acoustic propagation model to calculate paths of acoustic rays between the bottom-mounted sources and receivers as a function of time. We found that in many instances direct-path rays and single-surface bounce rays had arrival times very close to one another. This would have made it difficult to resolve these arrivals in field data due to finite source bandwidth. This was verified with actual field data, with the true environment often resulting in acoustic signatures that were even more complex than those predicted using model SSPs.

Our simulations using model results indicated that multiple surface bounce acoustic rays were stable in the path they took from source to receiver. Moreover, their arrival times were well separated from the early direct-path and single-surface bounce arrivals. As a result, their arrival times could be estimated fairly well. This provided a basis in our analysis of actual acoustic data for delineating times to consider for the arrival of rays traveling along specific paths. Moreover, multiple surface bounce rays provide a better sampling of the water column. Due to the drop in signal-to-noise for higher multiple surface bounce acoustic paths, we concentrated on analyzing paths that bounced off the ocean surface only twice.

Although acoustic simulation models are fairly accurate, they do have some limitations. For example, our modeling does not simulate the Doppler impacts of the motion of surface waves or surface roughness. However, simulations show that these factors can be effectively eliminated in the observations by averaging the arrival times over a number of pings that cover many cycles of surface motion. Another possible limitation is the error resulting from inaccuracies in the exact positions and depths of the source, receiver, and where a ray path bounces off the ocean bottom between the source and receiver.

Our analyses require a reference sound speed structure c_R. This was determined using monthly climatological T-S fields for the region shown in Fig. 1. Thus, c_R is a four-dimensional field with spatial resolution equal to that of the ocean circulation model and varying monthly. In addition, the PSAS assimilation scheme requires reference fields for T, S, and current velocities. Again, the monthly climatological T-S fields were used, while a reference velocity of 0 m/s was used throughout space and time.

B. Observed travel time anomalies

At a given time, an observed travel time t_o for a particular acoustic path can be combined with a reference ocean arrival time t_R to determine a *travel time anomaly*:

$$\Delta \tau_R = t_o - t_R. \tag{1}$$

The reference travel time is some predetermined standard derived by a computation of the travel time through the reference environment using a standard ray propagation model (e.g., Bellhop).

Any means of determining an observed travel time anomaly will include some measurement error, and we represent the errors associated with an observation as $\mathbf{e_z}(t)$:

$$\Delta \tau_{\text{True}} = \Delta \tau_R + \mathbf{e_z}. \tag{2}$$

C. Model-predicted travel time anomalies

We assume that the path of an acoustic ray of interest only deviates slightly from the path resulting from the reference sound speed structure, c_R, at any time. Thus, temporal changes in travel time are primarily associated with changes in propagation speed along the reference medium path (the "frozen ray" approximation). If we know the path an acoustic ray would take through the model domain (individual grid cells denoted by $i = 1,2,3,...,N$), we can calculate an estimated arrival time using

$$t_m = \Sigma [\Delta L_i / (c_{m,i} + U_{m,i})] \tag{3}$$

where the subscript m denotes model-predicted values, $c_{m,i}$ is the sound speed in the ith model grid cell, $\Delta L_{m,i}$ is the distance that the ray travels through the ith grid cell, and $U_{m,i}$ is the component of the three-dimensional current along a particular direction of interest responsible for effectively increasing or decreasing the sound speed. The model sound speed anomaly for each grid is

$$\Delta c_i = (c_{m,i} + U_{m,i}) - c_{R,i}, \tag{4}$$

where $c_{R,i}$ is based on reference T and S values.

Rearranging (4), substituting into (3), linearizing using $c_{Ri}^2 \gg \Delta c_i^2$, and rearranging the result in terms of a travel time anomaly (relative to the exact same t_R as in the expression for $\Delta \tau_R$) give

$$\Delta \tau_m(t) = -\sum_{i=1}^{N} \frac{\Delta L_i \Delta c_i(t)}{c_{R,i}^2} = \mathbf{b} \Delta \mathbf{c}^T, \tag{5}$$

where N is the number of model grid cells through which the ray travels. On the very right-hand side of (5), we have represented the summation as the multiplication of two vectors, $\mathbf{b}$ being the vector of the constant $-\Delta L_i / c_{R,i}^2$ terms and $\Delta \mathbf{c}$ being the vector of the time-varying terms $\Delta c_i(t)$.

As with the observed travel time anomaly, the model-predicted travel time has errors relative to the true value $\Delta \tau_{\text{True}}$:

$$\Delta \tau_{\text{True}} = \Delta \tau_m + e_{\text{DIS}}(t) + e_{\text{LIN}}(t) + e_{\text{TSU}}(t). \tag{6}$$

Errors due to the discretization process (representing $\Delta \tau_m$ by a summation over N grid cells as opposed to an integral over a continuum) are denoted by $e_{\text{DIS}}(t)$. The errors associated with the linearization approximation ($c_{Ri}^2 \gg \Delta c_i^2$) are contained in $e_{\text{LIN}}(t)$. The errors resulting from the differences between model-predicted sound speed (i.e., T, S, and U) and the true sound speed are denoted by $e_{\text{TSU}}(t)$.

The reader should note that we assume that the measurement error, $e_z(t)$, is a random variable that is uncorrelated with the model error terms.

D. The tomographic expression

Equation (5) must be transformed to relate travel time anomalies to ocean model variables (T, S, and $\mathbf{U}$). We express the sound speed in the ocean as a sum of a reference sound speed and a sound speed perturbation:

$$c = c_R + \frac{\partial c}{\partial T} \Delta T + \frac{\partial c}{\partial S} \Delta S + U = c_R + \delta c. \tag{7}$$

For local ocean temperatures and salinities and small temperature and salinity variations, we can approximate the two partial derivatives as

$$\frac{\partial c}{\partial T} \Delta T \approx 4.947 \Delta T = \alpha \Delta T, \quad \frac{\partial c}{\partial S} \Delta S \approx 1.34 \Delta S = \beta \Delta S,$$

where α has units of m/s/°C and β has units of m/s/ppt. We note that α and β are only gross approximations to $\partial c/\partial T$ and $\partial c/\partial S$, but their use is required to maintain the linearity of the set of expressions used in the assimilation process.

If the ocean model provides a reasonable first-guess of T, S, and U, we can rearrange (7) to give

$$\Delta c_i = \alpha \Delta T + \beta \Delta S + U \tag{8}$$

for every grid cell in the ocean model. We use (8) to transform (5):

$$\Delta \tau_m = \mathbf{b} \Delta \mathbf{v}^{\mathbf{T}} \tag{9}$$

where now

$$\mathbf{b} = [\, -\Delta L_1/c_{R,1}^2 \quad -\Delta L_1 \alpha/c_{R,1}^2 \quad -\Delta L_1 \beta/c_{R,1}^2 \quad \cdots$$
$$-\Delta L_N/c_{R,N}^2 \quad -\Delta L_N \alpha/c_{R,N}^2 \quad -\Delta L_N \beta/c_{R,N}^2 \,]$$

and the $\Delta \mathbf{v}$ vector is

$$\Delta \mathbf{v} = [\, U_1 \quad \Delta T_1 \quad \Delta S_1 \quad \cdots \quad U_N \quad \Delta T_N \quad \Delta S_N \,].$$

Each of the parameters in $\Delta \mathbf{v}$ is the model-predicted variable relative to the reference value, all of which are known. Essentially, (9) is our tomographic relationship, relating acoustic information to T, S, and $\mathbf{U}$.

We let the total number of rays present in any set of P source-receiver transects be M. We define $\mathbf{z}(t)$ as the column vector of the M travel time anomaly measurements ($\Delta \tau_R$'s) at time t. We define the matrix $\mathbf{H}$ as that whose rows are the above $\mathbf{b}$. Since each ray path may not go through the same number of grid cells N, the number of columns in $\mathbf{H}$ will be three times the maximum of the N's ($N_{\max}$), and there can be a number of zero entries in $\mathbf{H}$. Finally, we define $\mathbf{x}$ as the $3 \times N_{\max}$ column vector with the $\Delta \mathbf{v}$ for each grid cell through which a ray path travels.

We can relate all these matrices by the *measurement matrix residual equation*:

$$\mathbf{z}(t) - \mathbf{H}\mathbf{x}(t) = \text{residual}.$$

The goal of the data assimilation method is to minimize the residual. We note that, if the acoustic model grid is not co-incident with the ocean model grid, the measurement matrix $\mathbf{H}$ must be premultiplied by an interpolation matrix that maps the acoustic model grid onto the ocean model grid. In this study, the two grids coincide.

E. Assimilation of tomographic information into the ocean model

In our assimilation formulation, we define ocean parameters throughout the ocean model grid space as $\mathbf{x}$, $\mathbf{x}^{\mathbf{F}}$, and $\mathbf{x}^{\mathbf{A}}$ as vectors representing the *true state*, the *forecasted estimate* prior to assimilation, and the *analysis estimate* (after assimilation), respectively. The vectors $\mathbf{x}$, $\mathbf{x}^{\mathbf{F}}$, and $\mathbf{x}^{\mathbf{A}}$ are time dependent, and the three-dimensional T, S, and U fields form our state vector.

The basic expression we will use to determine the analysis (updated) field combines the forecast estimate $\mathbf{x}^{\mathbf{F}}$ with the acoustic-related measurements $\mathbf{z}_R$ (the $\Delta \tau_R$'s) using the model-related measurement matrix $\mathbf{H}$ as follows (the PSAS formulation):[5]

$$\mathbf{x}^{\mathbf{A}} = \mathbf{x}^{\mathbf{F}} + \mathbf{K}(\mathbf{z}_R - \mathbf{H}\mathbf{x}^{\mathbf{F}}). \tag{10}$$

As mentioned above, $\mathbf{z}_R - \mathbf{H}\mathbf{x}^{\mathbf{F}}$ is the measurement residual, the difference between the observation and the forecasted variable. $\mathbf{K}$ is the residual (Kalman) gain matrix:

$$\mathbf{K} = \mathbf{P}_{\mathbf{F}}\mathbf{H}^{\mathbf{T}}(\mathbf{H}\mathbf{P}_{\mathbf{F}}\mathbf{H}^{\mathbf{T}} + \mathbf{R})^{-1}.$$

$\mathbf{P}_{\mathbf{F}}$ is the spatial covariance of errors in the forecast, and $\mathbf{R}$ is the spatial covariance of errors in the observations. The formulations for these error matrices will be presented in the following section. But it is readily seen that, if $\mathbf{R} \gg \mathbf{H}\mathbf{P}_{\mathbf{F}}\mathbf{H}^{\mathbf{T}}$, the Kalman gain $\mathbf{K}$ approaches zero: $\mathbf{x}^{\mathbf{A}} = \mathbf{x}^{\mathbf{F}}$. Also, the Kalman gain distributes the measurement residual throughout the forecast model domain. The matrix $\mathbf{P}_{\mathbf{F}}$ can have values for each grid cell, and, thus, $\mathbf{K}$ will have a value for each grid cell, even for just one source-receiver pair. This is a significant advantage over inversion tomography where the covariance matrix tends to be limited to just the region being acoustically illuminated. Typically, corrections based on observations are assigned mostly to regions closest to the observations and areas where the forecast model error is the highest.

Note that $\mathbf{H}$ is used when determining $\mathbf{K}$ and during the assimilation process expressed in (10). Calculating $\mathbf{K}$ is performed prior to the assimilation process. Thus, even though we could use model-predicted T and S to obtain better estimates for $\partial c/\partial T$ and $\partial c/\partial S$ when employing (10), we do not have these values when calculating $\mathbf{K}$. This is the reason we employ the gross approximations of $\partial c/\partial T = \alpha$ and $\partial c/\partial S = \beta$, to make $\mathbf{H}$ consistent between the process of calculating $\mathbf{K}$ and then later using (10).

IV. SPECIFYING THE ERROR COVARIANCE MATRICES

For this preliminary study, (10) was simplified by assuming that travel time anomalies were primarily a result of the differences between predicted and ocean water temperatures. In this case, $\mathbf{x}^{\mathbf{F}}$ and $\mathbf{x}^{\mathbf{A}}$ are column vectors of forecasted and analysis temperatures relative to the monthly reference temperatures: $\mathbf{x}^{\mathbf{F}} = \mathbf{T}_{\text{model}} - \mathbf{T}_{\text{reference}}$ and $\mathbf{x}^{\mathbf{A}} = \mathbf{T}_{\text{analysis}} - \mathbf{T}_{\text{reference}}$. Since $\mathbf{T}_{\text{reference}}$ appears on both sides of (10), we see that the expression reduces to

$$\mathbf{T}_{\text{analysis}} = \mathbf{T}_{\text{model}} + \mathbf{K}(\mathbf{z}_R - \mathbf{H}\mathbf{x}^{\mathbf{F}}). \tag{11}$$

The rows of the $\mathbf{H}$ matrix now consist of

$$\mathbf{b} = [\, -\Delta L_1 \alpha/c_{R,1}^2 \quad -\Delta L_2 \alpha/c_{R,1}^2 \quad \cdots \quad -\Delta L_N \alpha/c_{R,N}^2 \,]$$

for each ray path. As before, $\mathbf{z}_R$ is the column vector of "observed" travel time anomalies. Thus, if $\mathbf{K}$ is properly determined, all the terms on the rhs of (11) are defined, and we can solve for $\mathbf{T}_{\text{analysis}}$.

A. Calculating the covariance functions

The modification of the model variables results from the application of (10). As such, the magnitude of the change of a model variable is critically dependent on the error covariance matrices. The model error covariance matrix is defined as

$$\mathbf{P}_{\mathbf{F}} = E[(\mathbf{x} - \mathbf{x}^{\mathbf{F}})(\mathbf{x} - \mathbf{x}^{\mathbf{F}})^T].$$

Of the various elements of $\mathbf{P_F}$, the e_{TSU} errors (differences between the model and the true ocean T, S, and $\mathbf{U}$) will likely be the most dominant. Typical values of sound speed in water and the magnitude of the rms errors determined from model/data comparisons (Sec. II B) indicate that the linearization error, e_{LIN}, is negligible: the value of c_{Ri}^2 will be at least four to five orders of magnitude larger than Δc_i^2, even with substantial errors in salinity. Numerical simulations suggest that discretizing the integral on the gridding scales used by the hydrodynamic model results in $e_{\text{DIS}} \leq 0.1$ ms for rays that interact with the surface one to three times. Thus, we ignore e_{DIS} and concentrate on developing a reasonable approximation for e_{TSU}.

The most accurate method of calculating the model error covariance matrix $\mathbf{P_F}$ is to use many realizations in space and time of model-predicted variables along with corresponding observations. Typically, such observations are nonexistent. One approach to deal with the lack of model-data comparisons is to estimate $\mathbf{P_F}$ by the spatial covariance from the time sequence of the model-predicted variable over a set of (x,y,z) locations:[16]

$$\mathbf{P_F} = E[(\mathbf{T}_{\text{MODEL}} - E[\mathbf{T}_{\text{MODEL}}])(\mathbf{T}_{\text{MODEL}} - E[\mathbf{T}_{\text{MODEL}}])^T]. \qquad (12)$$

It is easily shown that the model covariance equals the sum of the model error covariance plus the covariance of the true state of the ocean. Thus, $\mathbf{P_F}$ given by (12) always results in overestimating the error covariance. As a result, the rate of spatial decorrelation of the errors of a variable can be underestimated. Therefore we would expect the observations to be more spatially limited in their impact on the analysis fields, which in itself is not an adverse consequence but may not make full use of the observations.

A second method involves estimating the error covariance matrix $\mathbf{P_F}$ utilizing scaled, time histories of model-predicted temperatures. In the first step of this method, a time series of errors is specified for a given temperature $T(x,y,z,t)$ as

$$T_{\text{error}}(x,y,z,t) = T(x,y,z,t + 24 \text{ hours}) - T(x,y,z,t).$$

Using the 24-h offset, the "errors" are simply a result of day-to-day variability in atmospheric forcing, the phase of the tides, wave conditions, and the MODAS T-S fields. From this we can calculate n days worth of estimates of errors (for our study, errors at hourly intervals) for the ocean variable T. The second step is the scaling of the errors T_{error}. This scaling process relies on the existence of model predictions and corresponding observations with which to calculate an rms model error. In our case, 175 bathythermographs were used to calculate an rms error for T as a function of depth. Thus, each $T_{\text{error}}(x,y,t)$ for a specific z can be scaled [each value of $T_{\text{error}}(x,y,z,t)$ increased or decreased] so that the model-model rms errors match the observed-model rms errors. This scaling allows us to produce estimates between the model and the true state of the ocean that are realistic in that the rms model-model differences match rms model-data differences. We use the scaled time histories to calculate the appropriate spatial covariance matrix using

$$\mathbf{P_F} = E[(\mathbf{T}_{\text{error}} - E[\mathbf{T}_{\text{error}}])(\mathbf{T}_{\text{error}} - E[\mathbf{T}_{\text{error}}])^T]. \qquad (13)$$

Another consideration is the length of the time series over which the spatial covariance is calculated. Commonly, the spatial correlation structure varies with factors such as the phase of the internal tides. Thus, the error covariance matrices should be recalculated on a fairly regular basis. The time span over which $\mathbf{T}_{\text{MODEL}}$ or $\mathbf{T}_{\text{error}}$ extend should partially reflect conditions during which travel time anomalies are to be assimilated. If the fortnightly phase of the internal tide is the primary factor controlling spatial structure, then a time series of ~ 3 days may be appropriate. In this study, we consider estimates of the model covariance matrix using 3 days of hourly data.

The observation error covariance matrix is defined as

$$\mathbf{R} = E[(\mathbf{e_z} + E[\mathbf{e_z}])(\mathbf{e_z} + E[\mathbf{e_z}])^T].$$

There are two components of the measurement error vector $\mathbf{e_z}$. The first component is given by

$$\sigma_t = \frac{1}{bw\sqrt{\text{SNR}}},$$

where bw is the bandwidth of the signal ($bw = 2\pi\Delta f$) and SNR is the signal-to-noise ratio. In our experiment performed at PMRF during June–July 2003, we had a bandwidth of 3000 Hz. Assuming a signal-to-noise ratio of 10 dB, this error is around 32 μs.

The second component of $\mathbf{e_z}$ is due to the fluctuations in the water column temperature and salinity, the roughness of the ocean surface, and uncertainties in the bathymetry. One approach to estimate this error is from the acoustic data itself. This is done by estimating the standard deviation of the arrivals for a set of pings between a source-receiver pair. This information is presented in the following section.

B. Implementation

In implementing our data assimilation scheme, we limited the model grid cells impacted by acoustic observations to those within 20 km of any model grid cell through which ray paths being considered traveled. This reduced the number of covariance functions that had to be calculated. If L_{max} is the number of grid cells within the 20-km range, then $\mathbf{P_F}\mathbf{H}^T$ for the p ray is an L_{max} column vector. There are 12 monthly column vectors ($\mathbf{c_R}$ for a given grid cell varies by month) for the any ray path. All the elements were calculated and stored in a database. Similarly, all terms in the $\mathbf{HP_F}\mathbf{H}^T$ matrix are known, and each monthly matrix was calculated. The monthly $\mathbf{HP_F}\mathbf{H}^T$ matrices were inverted and multiplied by $\mathbf{P_F}\mathbf{H}^T$ to give 12 $L_{\text{max}} \times P_{\text{max}}$ arrays, where P_{max} is the number of ray paths being considered (i.e., there are P_{max} arrival time anomalies).

Thus, the analysis and assimilation software only requires the monthly databases of (1) the $\mathbf{P_F}\mathbf{H}^T(\mathbf{HP_F}\mathbf{H}^T)^{-1}$ elements, (2) the reference temperatures along the acoustic paths being considered [for Δv in (9)], and (3) the $-\alpha\Delta L_N / c_{R,N}^2$ values [for $\mathbf{b}$ in (9)].

As in any assimilation scheme, there are additional factors that have been incorporated in our process. First, we
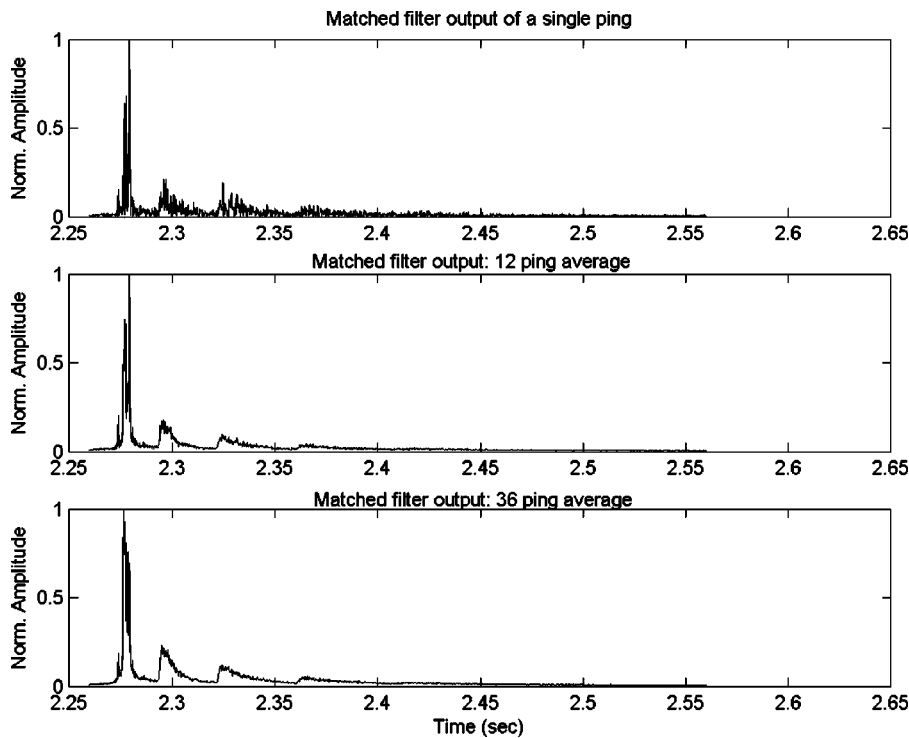
FIG. 2. Matched filter output for a single transmission (top), an average of 12 transmissions (middle), and an average of 36 transmissions (bottom).

assumed that the MODAS temperature field, $T_M(x,y,z)$, reflects a norm for the $\mathbf{T}_{analysis}(x,y,z)$ field. We used the 175 bathythermographs (Sec. II B) to calculate relative ranges for each vertical level of the ocean model: $Ra(z)=T(z)_{max}-T(z)_{min}$. We then limited the replacement of the elements in the $\mathbf{T}_{model}$ field to those grid cells in which the assimilation process resulted in (a) a water temperature within the range of $T_M(x,y,z)\pm Ra(z)/2$, (b) a water temperature closer to $T_M(x,y,z)-Ra(z)/2$ when $\mathbf{T}_{model}<T_M(x,y,z)-Ra(z)/2$, or (c) a water temperature closer to $T_M(x,y,z)+Ra(z)/2$ when $\mathbf{T}_{model}>T_M(x,y,z)+Ra(z)/2$. These limitations were found to aid in preventing the assimilation process from making model-predicted temperatures that were already too cold (warm) from being made even colder (warmer). This is not to say that other forcings cannot result in model-predicted temperatures that drift away from the $T_M(x,y,z)\pm Ra(z)/2$ field. Only the assimilation process is constrained to alter the model-predicted temperatures toward a range about the MODAS temperatures.

V. THE ACOUSTIC DATA

Each signal transmitted from a PMRF source is acquired by an acoustic data acquisition system (ADAS) at designated receivers. The transmitted signal is then replica-correlated with the received signal. The received signal is modeled as a sum of ray arrivals given by

$$r(t)=\sum_n a_n s(t-\tau_n),$$

where a_n is the weight associated with each arrival, $s(t)$ is the transmitted signal, and τ_n is the delay associated with each arrival. When correlated with the transmitted signal, the output will have peaks at times corresponding to the travel times of eigenrays between the source and receiver. There

are two sources of error in the estimation of travel time if we use the above representation. First, the sound channel is dispersive, and we cannot expect the transmitted signal shape to remain unchanged as it propagates through the channel. The second error is because we have not correctly modeled phase changes that occur during propagation (due to caustics or boundary reflections). Simulations show that the errors in arrival time estimates due to both these causes are of the order of tens of microseconds, which is less than the error in arrival time estimates as a result of the finite source bandwidth. Thus, these errors can be ignored for our application.

Two candidate transmit signals were tested: a linear chirp and a 511-digit m-sequence. In areas where the acoustic signal interacts with waves on the ocean surface, there can be a Doppler shift that compresses or elongates the signal envelope, depending on the direction of motion of the ocean surface relative to the incident acoustic energy. Matched filter output of this Doppler-shifted signal gives rise to errors in (a) estimating the arrival time and (b) the amplitude of the matched filter output of each arrival. Analysis of the errors in estimating arrival times showed that the errors in the phase-coded sequence were less than that of the chirp signal. However, the amplitude of the matched filter output remained practically unaltered in the case of chirp signal, while in the phase-coded sequence it is reduced substantially. This resulted in greater difficulties in detecting a phase-coded signal in the presence of background noise. Since averaging can eliminate the error in the arrival time due to surface motion, the transmissions used in this study were chirp signals with a center frequency of 9.5 kHz and a bandwidth of 3 kHz.

To improve the signal-to-noise ratio and to reduce the impact of surface motion, we averaged over a number of acoustic transmissions. Under normal circumstances, it would have been appropriate to send a large train of acoustic
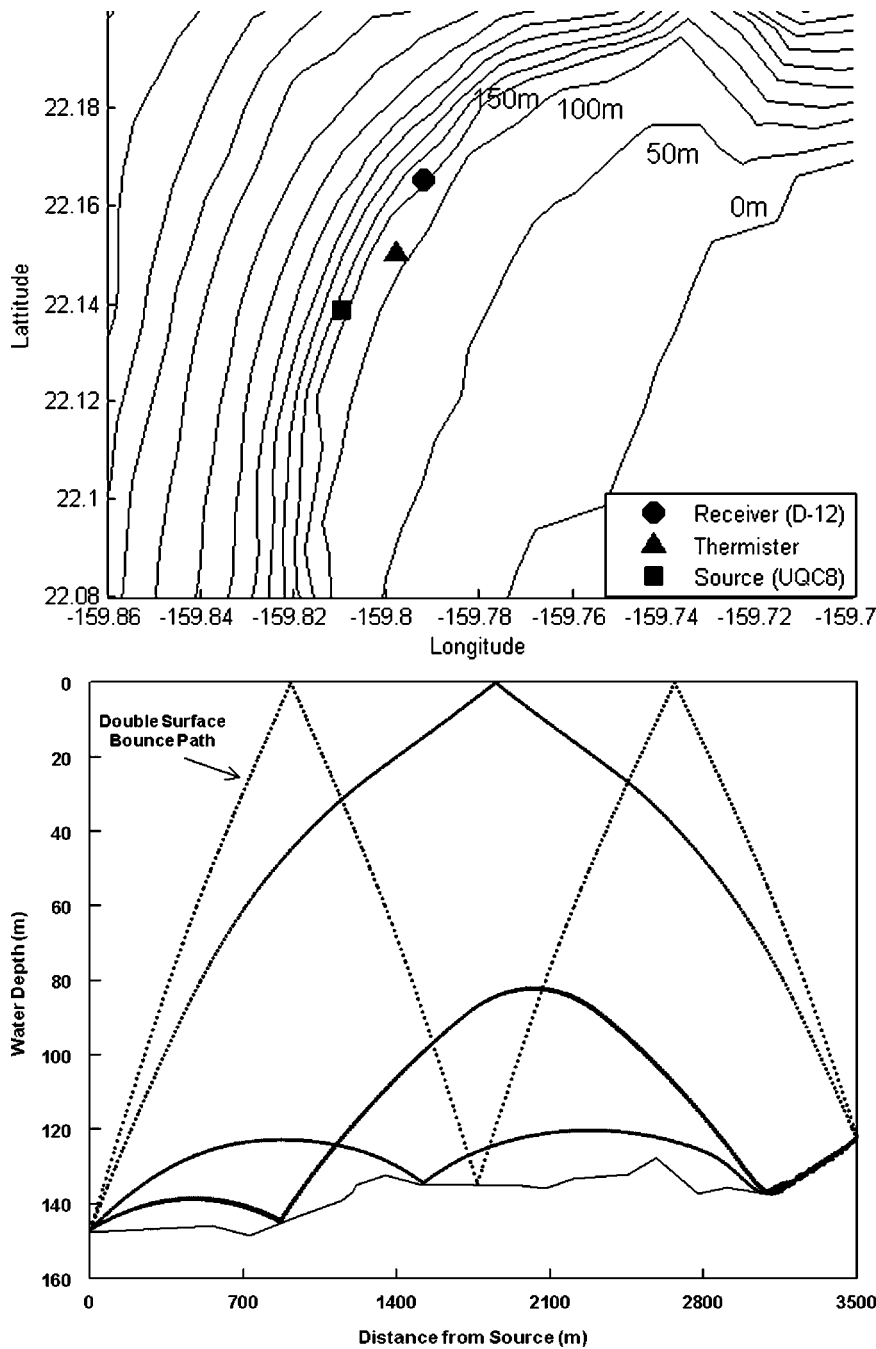
FIG. 3. Top panel—bathymetry and locations of the source (*), receiver (○), and where thermistor data were collected (△). Bottom panel—examples of ray paths between the source and receiver.

pulses and perform an average over this train of pulses. However, this was not possible because of "cross talk" between the transmitter and receivers at PMRF. Instead, we transmitted a sequence of 12 acoustic transmissions that consisted of four groups separated by 8 s. Each acoustic transmission had a duration of 0.1 s, with an interval of 0.4 s between each transmission. The number of pulses in a group was restricted to three transmissions to avoid interference due to the cross talk. The distance to the nearest receiver set this limitation. The maximum distance between the source and selected receivers dictated the 8-s separation between groups of transmissions. The string of 12 transmissions was repeated three times with an interval of about 30 s. The length of each train of pulses (i.e., about 28 s) and the time interval between each train were selected on the basis of the requirements of the data acquisition system.

The matched filter outputs for a varying number of transmissions are shown in Fig. 2. The top panel shows the output using only one transmission. The output using the average of 12 transmissions is shown in the middle panel, and the output using the average of 36 transmissions is shown in the lower panel. We see that a considerable enhancement of the signal-to-noise ratio is achieved by averaging over 36 transmissions.

The arrival structure in Fig. 2 consists of one stronger arrival followed by three weaker arrivals. An eigenray[17] analysis for this particular source/receiver pair was performed using a sound speed field for the region obtained from the ocean model. Based on this analysis, the earliest group of arrivals consists of rays that travel from source to receiver without interacting with either the ocean surface or bottom and others that include a ray that interacts with the
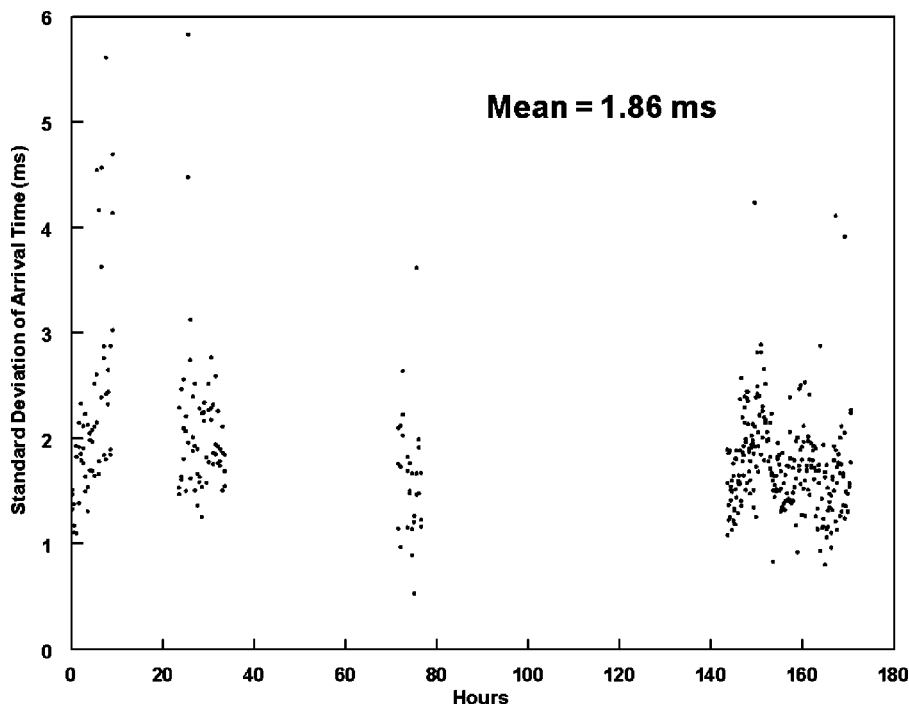
FIG. 4. Standard deviation of the arrival times for acoustic data between PMRF hydrophones D9 and D12 during late June and early July 2003 at PMRF.

surface only once and rays that hug the bottom and have repeated interactions with the bottom. The arrival times of rays that have only interactions with the bottom carry little information about the bulk of the water column. This plus the problem of delineating individual ray arrival times within the first group of arrivals lead us to neglect these arrivals in our tomography analysis.

The subsequent three arrivals in Fig. 2 correspond to rays that have two, three, and four surface bounces, respectively. As mentioned before, we concentrated on analyzing the path that bounced off the ocean surface only twice due to the drop in signal-to-noise for higher multiple surface bounce acoustic paths (the third and fourth arrivals).

For the initial development and testing of this technology, we worked with just one ray path. The ADAS was used to collect travel time observations for a double-surface bounce ray path at PMRF just offshore of the 90-m isobath (Fig. 3). The ray path was between a bottom-mounted source (D9) some 3.5 km from a bottom-mounted receiver (D12). From an eigenray analysis performed using a mean sound speed structure for the area, the arrival time of a ray with two surface bounces is about 2.3 s. This is used to readily identify the arrival time of the two-surface bounce ray in the ADAS data (Fig. 2). An enhanced view (not shown) of the
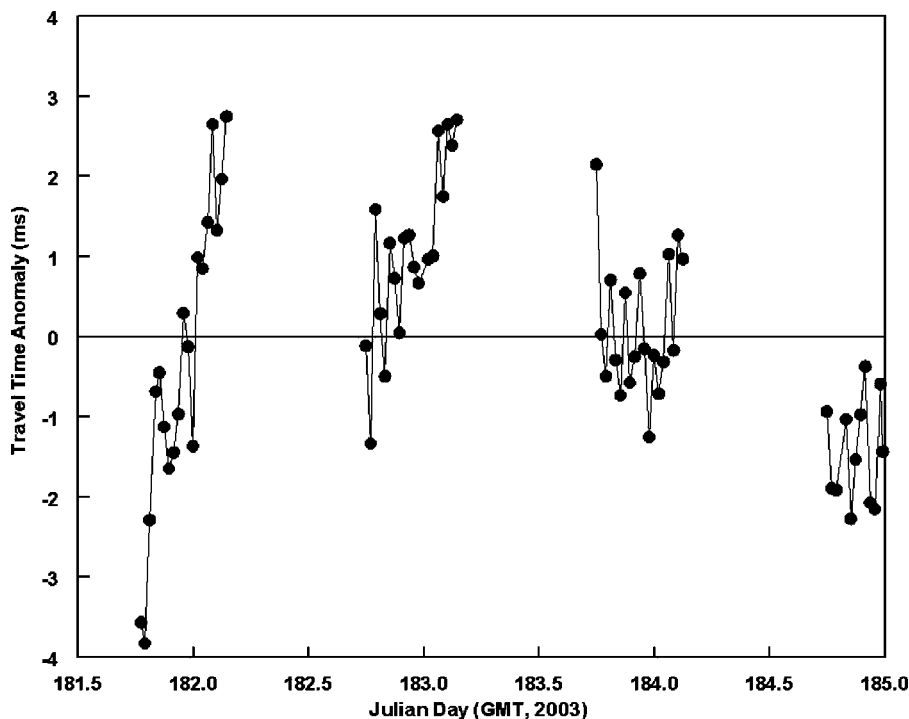

FIG. 5. Calculated travel time anomalies for a two-surface bounce ray path over a 3.5-km distance between the PMRF source D9 and receiver D12.
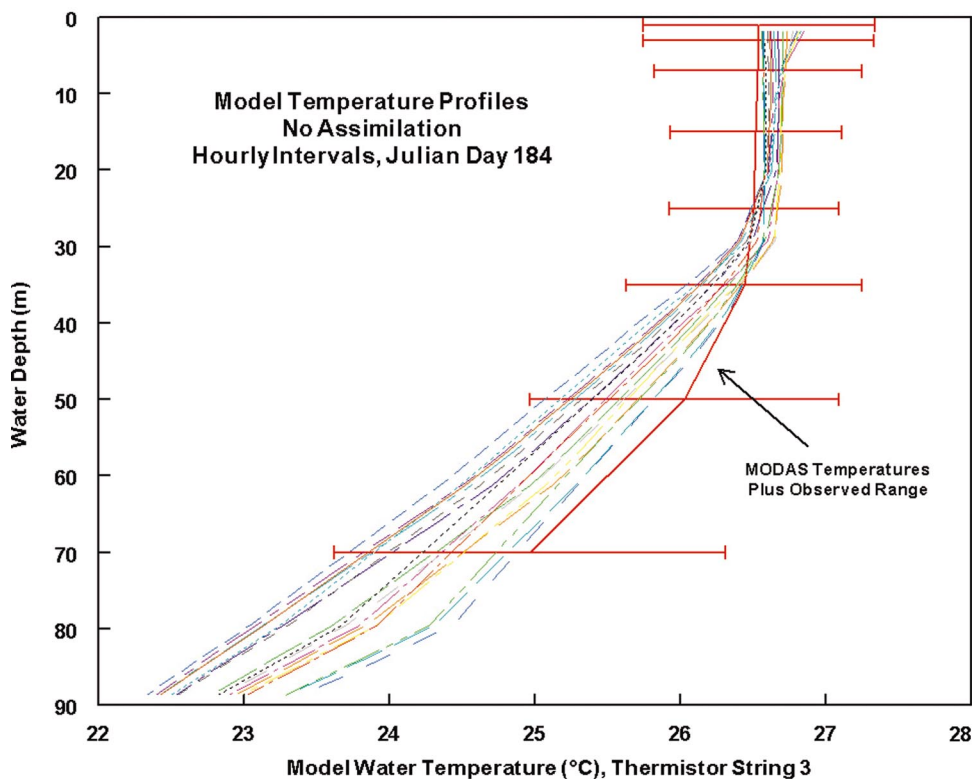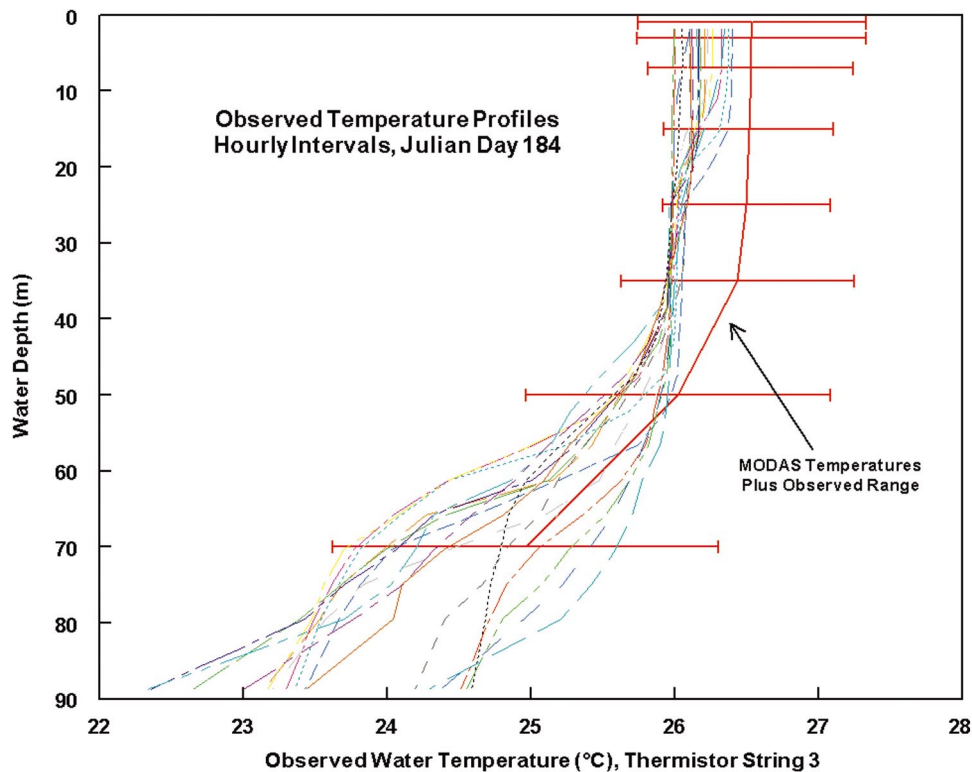
FIG. 6. Hourly temperature profiles for 3 July 2003 at the thermistor site shown in Fig. 3: observed (top) and predicted, no assimilation (bottom). The MODAS temperature profiles for that date and location are also shown (solid red), along with the observed ranges of temperatures (horizontal solid red) determined from the 178 BTs, centered on the MODAS temperatures.

matched filter output corresponding to the arrival time for this ray indicates multiple peaks that are likely the result of the roughness of the ocean surface and the ocean bottom. In order to determine the arrival time of a particular ray, we performed cluster analysis of the arrival times and their relative amplitudes of all arrivals that represented the acoustic ray of interest. The centroid of the cluster of peaks was used as the estimate of the arrival time. In addition, the variance

of the cluster of peaks (arrival times) was used to estimate the error covariance matrix $\mathbf{R}$.

The data were used to estimate the $\mathbf{e_z}$ error term for the two-surface bounce ray between D9 and D12. The standard deviations of the all arrivals for sets of pings covering a 180-h period are shown in Fig. 4. As can be seen, there is a significant amount of variability in the standard deviation, varying from 0.5 to 6 ms. The mean was 1.8 ms. We note
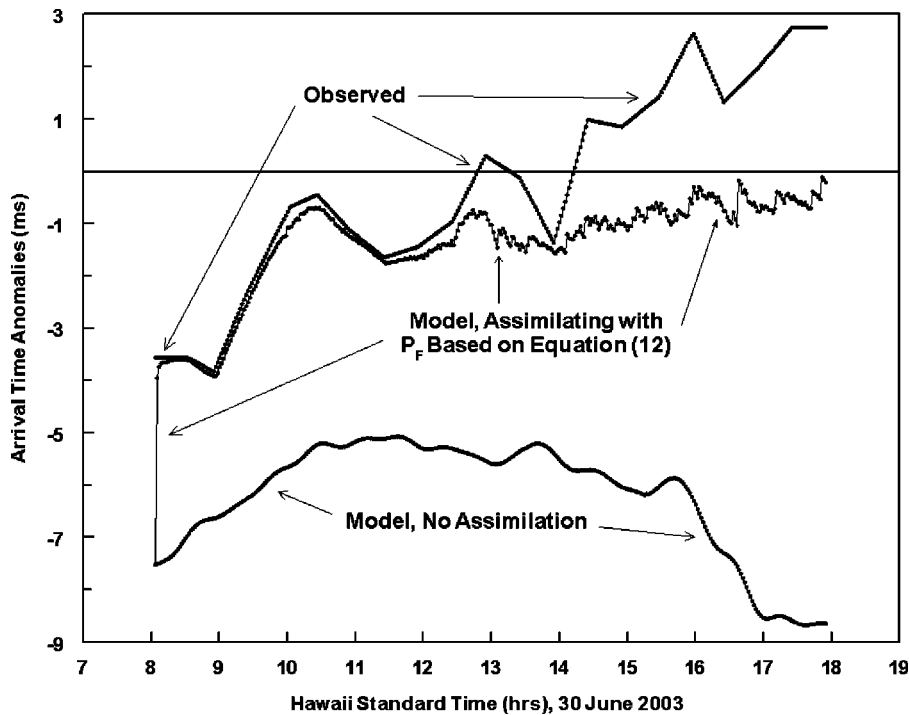
FIG. 7. Observed travel time anomalies (z_R) and model-predicted travel time anomalies ($\mathbf{Hx^F}$) using (12). Each dot represents one time step (100 s) of the numerical ocean model. The variations of $\mathbf{Hx^F}$ with $\mathbf{K}=0$ (no assimilation) are shown by the bottom curve.

that this $\mathbf{e_z}$ error is orders of magnitude greater than the σ_t error due to noise in the signal and the limited bandwidth of the signal (32 μs). Thus, we can neglect σ_t.

VI. DATA ASSIMILATION TEST CASE, JULY 2003

During an Office of Naval Research experiment[18] at PMRF during June–July 2003, a series of thermistor strings were placed along the 90-m isobath just shoreward of the D9-D12 source-receiver pair. The distance between the D9-D12 ray path and the thermistor arrays was ~0.5 km. As

such, the thermistor data provide a means of assessing the impact of assimilating the D9-D12 arrival time anomaly data into the ocean circulation model.

During 30 June–3 July 2003, the ADAS was used to generate 8–11-kHz chirps (linear FM sweep) with a duration of 100 ms from D9. The signal was transmitted 36 times over a 2.5-min period every half hour. Data were collected from about 8:00 AM to about 5:00 PM local time (1800 GMT to 0300 GMT) for all 4 days. Output of each transmission in the three chirp trains was run through the matched filter process, and then the 36-transmission average was calculated. In
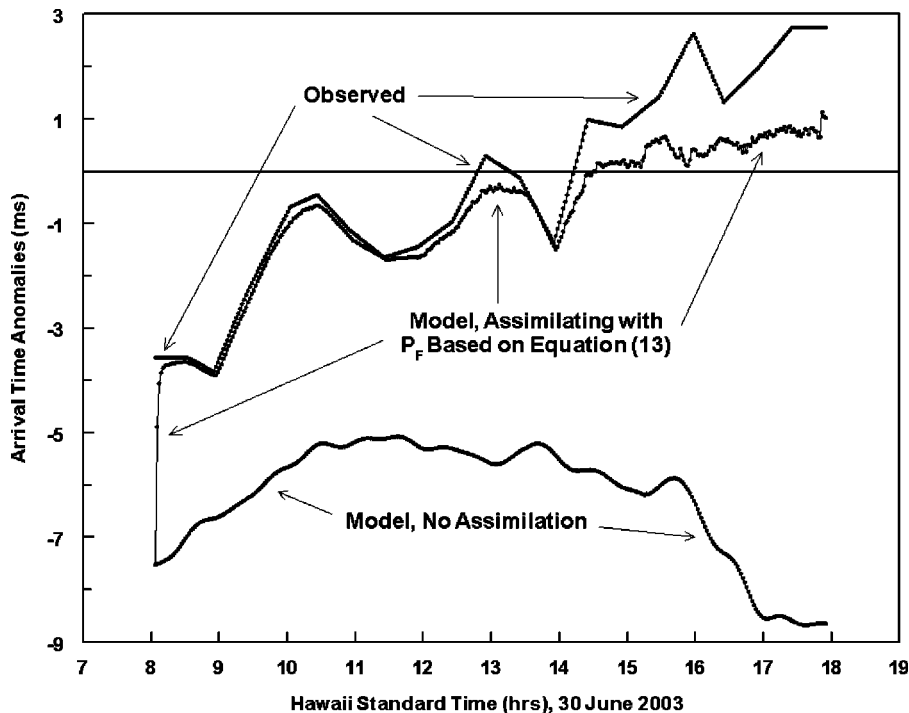

FIG. 8. Observed travel time anomalies (z_R) and model-predicted travel time anomalies ($\mathbf{Hx^F}$) using (13). Each dot represents one time step (100 s) of the numerical ocean model. The variations of $\mathbf{Hx^F}$ with $\mathbf{K}=0$ (no assimilation) are shown by the bottom curve.
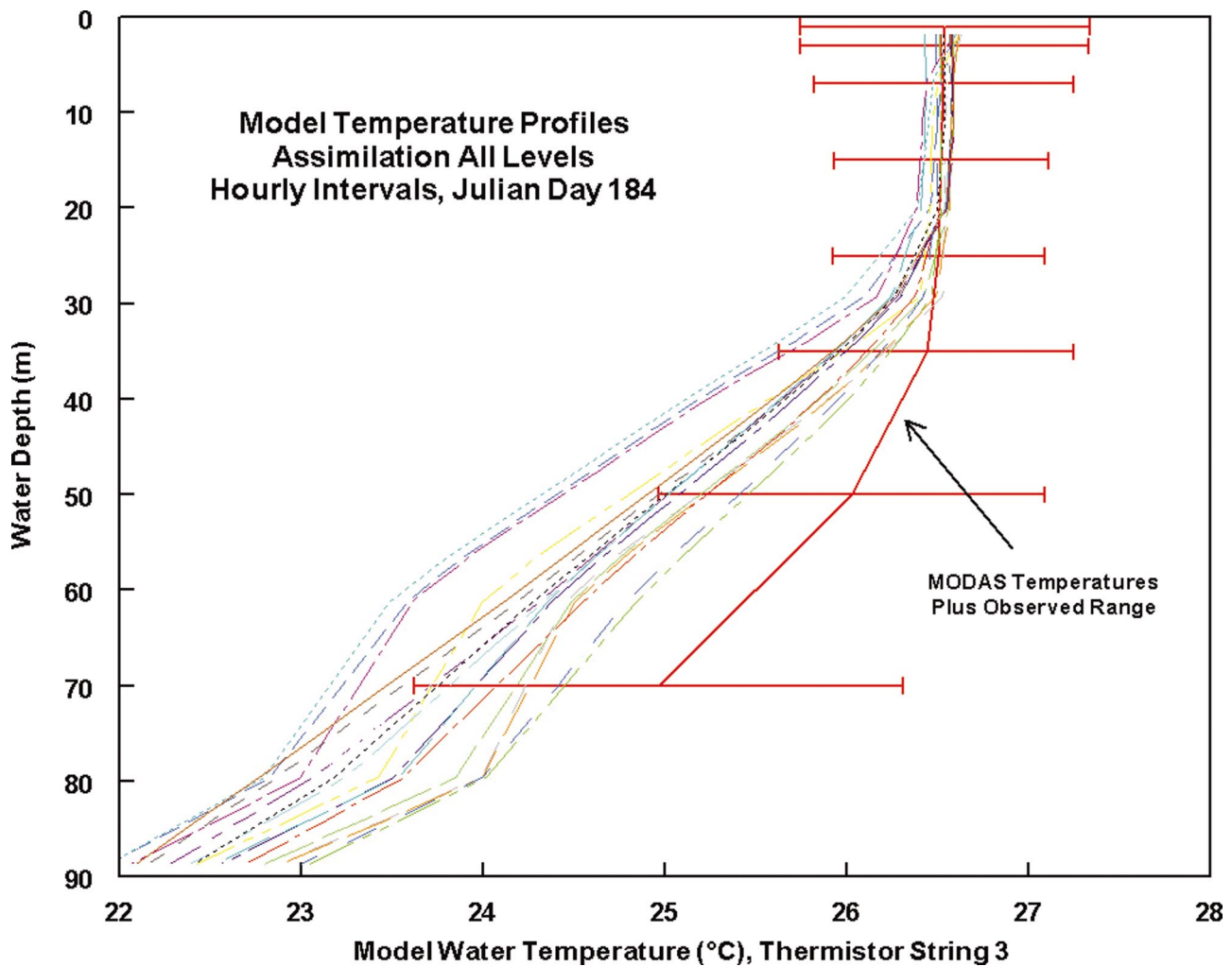
FIG. 9. Model-predicted hourly temperature profiles for 3 July 2003 at the thermistor site shown in Fig. 3. The MODAS temperature profiles for that date and location are also shown (solid red), along with the observed ranges of temperatures (horizontal solid red) determined from the 178 BTs, centered on the MODAS temperatures.

cases where multiple peaks resulted in an ambiguity in determining the arrival time, the averaged matched filter output was low-pass filtered.

After determining all the arrival times of the double surface bounce path between D9 and D12, travel time anomalies were calculated for assimilation into the ocean model. These are shown in Fig. 5. There are distinct longer-term variations in arrival time anomalies that are likely a result of tidal fluctuations and/or surface heating and cooling. But the observed travel time anomalies also have large hour-to-hour variations. These short-term fluctuations could be the result of signal processing (i.e., the ''noise'' seen in the curves in Fig. 2) or actual ocean processes that alter the sound speed of the water column. When translated to geophysical fluid dynamics, the short-term variations mean short space scale phenomena: e.g., solitons. Even if these fluctuations are not a result of signal processing, our ocean model does not have the horizontal resolution (tens of meters) that would be required to reproduce such short space scale phenomena. To mitigate the impact of such fluctuations in the arrival time anomalies (which would generate spurious gravity waves in the ocean model), we limit the magnitude of any changes to the model-predicted temperatures to be $<2.7\times10^{-4}$ °C/s for

each time step. This would still allow up to a 5–6 °C temperature change over a 6-h period, a not-uncommon signature of internal tides around the Hawaiian Islands.

The ocean model was first executed without any acoustic data assimilation, and the model-predicted water temperatures were compared to the thermistor data. A comparison of the model-predicted and observed water temperatures at the site shown in Fig. 3 on 3 July 2003 is shown in Fig. 6. There is a distinct bias in the surface mixed layer (observed temperatures>26 °C) where the model-predicted temperatures are too warm. For the cooler waters at depth, the scatter is considerable, with the model predictions being as much as about 0.8 °C too warm and 2.2 °C too cool.

A. Tests of assimilation parameters

We used $e_z = 1.86$ ms, or $R = (1.86\times10^{-3} \text{ s})^2 = 3.46 \times 10^{-6} \text{ s}^2$. For estimating P_F, we have put forth two possible methods: those in Eqs. (12) and (13). As a measure of quantifying the magnitude of the impact of assimilating the acoustic information for different P_F's, we compared the two quantities of the measurement residual, z_R and Hx^F. Recall that z_R is the observed travel time anomaly (Fig. 5) and Hx^F

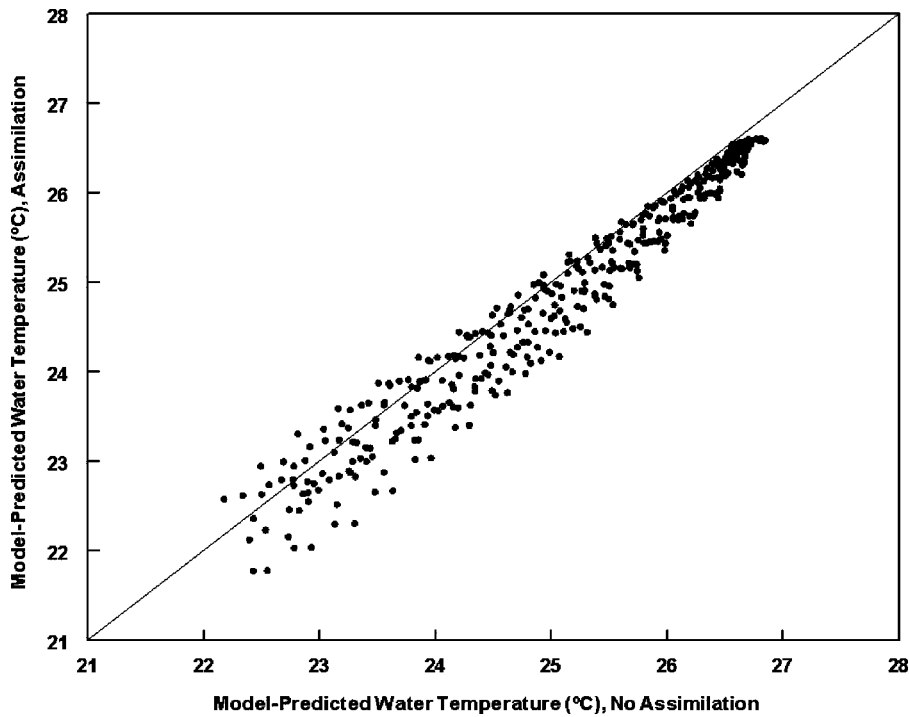Lewis *et al.*: Model-oriented ocean tomography

FIG. 10. A scatter plot of model-predicted water temperatures at one of the thermistor strings for 3 July 2003, with (ordinate) and without (abscissa) assimilation. Points below the diagonal line indicate that the assimilation process resulted in cooling.

is the corresponding travel time anomaly predicted by the ocean model. If the effect of the assimilation is significant, then $\mathbf{H}\mathbf{x}^F \rightarrow \mathbf{z}_R$ over time.

We first used $\mathbf{P}_F$ as defined in Eq. (12) with the time series used to calculate $\mathbf{P}_F$ being 72 h of temperatures for each model grid cell. An example of the variations of $\mathbf{H}\mathbf{x}^F$ and $\mathbf{z}_R$ is shown in Fig. 7. Each dot in Fig. 7 represents one time step of the ocean model (100 s). When the assimilation process started, $\mathbf{H}\mathbf{x}^F$ was approximately twice as large as $\mathbf{z}_R$, with about a 4-ms difference between the two. Within three time steps (and, thus, three new sets of $\mathbf{T}_{\text{analysis}}$ ingested by the model), $\mathbf{H}\mathbf{x}^F$ was reproducing $\mathbf{z}_R$ quite well. This good reproduction continued for the next 3–4 h. By about 12:45 hours local time, the difference between $\mathbf{z}_R$ and $\mathbf{H}\mathbf{x}^F$ began to increase, reaching a maximum of the order of 3+ ms by 18:00 hours local time.

A similar test was conducted using $\mathbf{P}_F$ as defined in (13), and the results are shown in Fig. 8. As before, the assimilation initially resulted in a good reproduction of $\mathbf{z}_R$. But, in this case, the good reproduction lasted longer, for about 6.5 h. By 15:00 hours local time, the differences between $\mathbf{z}_R$ and $\mathbf{H}\mathbf{x}^F$ became larger but were noticeably smaller than those shown in Fig. 7. By 18:00 hours, the differences were of the order of 2 ms.

We note that, as the differences between $\mathbf{z}_R$ and $\mathbf{H}\mathbf{x}^F$ in Figs. 7 and 8 increase, $\mathbf{H}\mathbf{x}^F$ is characterized by higher frequency oscillations. This type of variability commonly indicates that other model forcing (e.g., tidal, atmospheric, etc.) is substantial enough to counter the adjustments resulting from assimilating the observed travel time anomalies, thus explaining the increasing differences between $\mathbf{z}_R$ and $\mathbf{H}\mathbf{x}^F$. The bottom curves in Figs. 7 and 8 show $\mathbf{H}\mathbf{x}^F$ with no assimilation. It is obvious that one of the other forcings is pushing $\mathbf{H}\mathbf{x}^F$ to become more negative after about 14:00

hours, with a strong negative trend after 15:30 hours. This is opposite to the trend of $\mathbf{z}_R$.

Based on the results shown in Figs. 7 and 8, we use Eq. (13) for defining $\mathbf{P}_F$ for our assimilation exercises. In doing so, we calculated the value of $\mathbf{H}\mathbf{P}_F\mathbf{H}^T$ for the single acoustic path between D9 and D12. This value was 7.01×10^{-6} s². Thus, $\mathbf{H}\mathbf{P}_F\mathbf{H}^T$ was about twice that of $\mathbf{R}$ (3.46×10^{-6} s²).

B. Impact of assimilation process, 3 July 2003

Simulations were performed with the assimilation procedure executed whenever there were any arrival time anomaly data within 0.5 h of the model simulation time. The $\mathbf{P}_F$ matrix was determined using (13) with 3 days of hourly model results. In Fig. 9 we show the model temperatures at the same thermistor string whose data are shown in Fig. 6 (top panel). We see that the assimilation process resulted in cooler surface waters, but the warmer surface bias still exists. It is apparent that the assimilation lowered the subsurface water temperatures also (observed temperatures $< 26\,°\text{C}$), with the maximum overprediction in deeper waters being reduced to $+0.5\,°\text{C}$. However, the model temperatures in the lower part of the water column were lowered too much, with underpredictions being now as large as $-2.3\,°\text{C}$.

The overall impact of the data assimilation is better depicted in Fig. 10. In general, the temperatures of the water column were lowered (points below the diagonal line), with the cooling being larger in magnitude as the depth increased (toward the left-hand side of Fig. 10). We also see that the assimilation process resulted in some increasing temperatures (points above the diagonal) further down in the water column. The assimilation process induced relatively modest temperature changes for the 24-h period of 3 July 2003, ranging from $+0.5$ to $-0.8\,°\text{C}$.
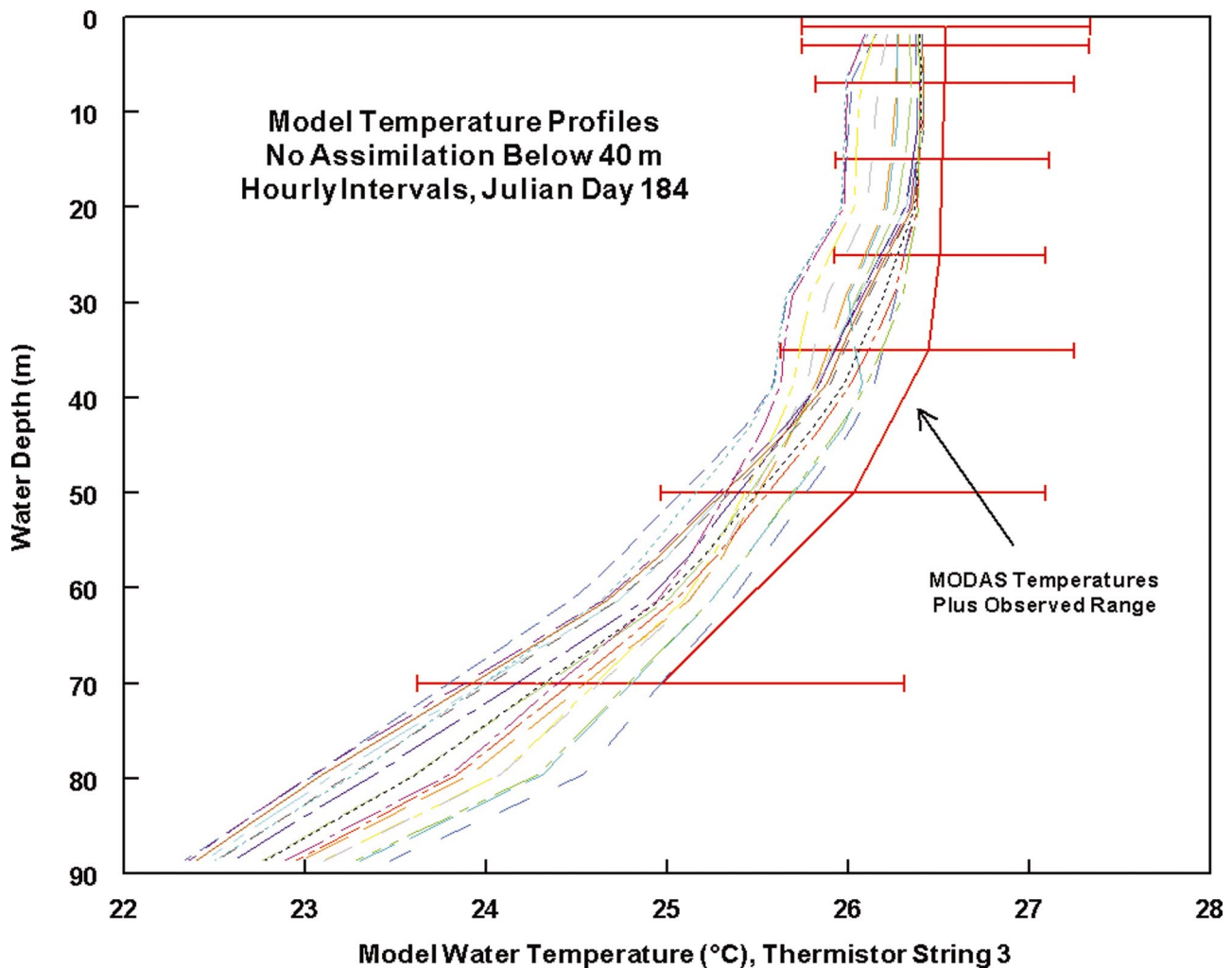
FIG. 11. Model-predicted hourly temperature profiles for 3 July 2003 at the thermistor site shown in Fig. 3. The MODAS temperature profiles for that date and location are also shown (solid red), along with the observed ranges of temperatures (horizontal solid red) determined from the 178 BTs, centered on the MODAS temperatures.

Comparing Figs. 6 and 9, we would conclude that assimilating the one ray path had both positive and negative impacts. On the positive side, the acoustic information reduced the number of occurrences in which the model-predicted water temperatures were too warm. However, the assimilation failed to eliminate the warm bias of the model predictions near the ocean surface and actually accentuated the cool bias of the model in the lower parts of the water column.

The warm bias of the model near the ocean surface was a persistent feature for 30 June–3 July 2003. Using this fact, we modified our process such that assimilation occurred only over the top 40 m of the ocean model. No adjustments based on the acoustic data were made below 40 m. The resulting temperature profiles are shown in Fig. 11, and these can be compared to the profiles in Figs. 6 and 9. We see that model-predicted near-surface temperatures better reflect the observed temperatures, both in magnitude and variability. The lower layers of the water column were still too cool, but the assimilation process did not accentuate this bias in this test.

VII. SUMMARY AND CONCLUSIONS

We have presented a model-oriented acoustic inversion and assimilation technique for arrival time anomalies from bottom-mounted sources and receivers. In calculating an observed arrival time, we attempted to eliminate the impacts of Doppler shifts and scattering at the ocean surface by averaging over a number of pings. The reference arrival time between a source-receiver pair was calculated using an acoustic propagation model based on model-predicted SSPs, the specified locations and depths of the source and receiver, and the available bathymetry between the source and receiver.

The arrival time anomalies from only one acoustic path were used in a test of this technology at PMRF in Hawaii. When assimilating over all model grid cells, the acoustic information helped in reducing the number of occurrences in which the model-predicted water temperatures were too warm. However, the assimilation technology for this case introduced a distinct cool bias in the lower levels of the water column (Fig. 9). A second test used the fact that the model near-surface temperatures at the location of the observations were consistently too warm, so assimilation occurred only over the top 40 m of the water column. In this case, knowledge of the model bias allowed the technology to result in better near-surface predictions without enhancing the bias in the lower layers of the water column.

In the first test, the changes in the character of the pro-

files (Figs. 6 and 9) are readily explained by the values calculated for the Kalman gain matrix $\mathbf{K}$. When dealing with only one ray path, there is a single element of the matrix $\mathbf{K}$ for each model grid cell. This is multiplied times the corresponding element of $\mathbf{z}_R - \mathbf{Hx^F}$ (which itself will be a scalar for a single ray path). Thus, a larger value of the element of $\mathbf{K}$ for a grid cell results in a greater modification in the model-predicted water temperature in that grid cell during the PSAS assimilation process. An analysis of $\mathbf{K}$ showed that larger values were associated with water depths from 80 to 300 m. As a result, the assimilation of travel time anomalies had the greatest impact on the lower levels of the model grid cells. This differential impact is quite evident when we consider Fig. 10.

Because of the smaller values of the Kalman gain, the surface layers were not cooled fast enough before the lower layers were cooled so much that the model-predicted arrival time anomaly matches the observed arrival time anomaly. The result is the overcooling of temperatures in lower levels of the model (the more prominent cold bias in Fig. 9 when compared to Fig. 6) and the continuing warm surface bias for the model results.

Since the PSAS assimilation scheme is critically dependent on the Kalman gain matrix $\mathbf{K}$, we have attempted to make reasonable estimates of the model and observation error covariance matrices. For $\mathbf{P_F}$, the scaled error approach [Eq. (13)] appears to work better than $\mathbf{P_F}$ calculated using the model covariances [Eq. (12)]. For $\mathbf{R}$, the use of the standard deviation of the observed arrival times provides a practical means for determining the component $\mathbf{e_z}$. The results using our estimates of $\mathbf{P_F}$ and $\mathbf{R}$ appear to provide a good assimilation methodology of the observed travel time anomalies (Fig. 8).

It is obvious that additional work is needed in applying modifications to individual model grid cells based on travel time information from bottom-mounted hydrophones. Utilizing higher frequencies means sampling conditions throughout the water column over relatively short distances (3–5 km). This is advantageous in that multiple surface bounce ray paths from bottom-mounted hydrophones are relatively stable and are integrating over horizontal scales across which T, S, and $\mathbf{U}$ tend not to vary by large amounts. On the other hand, there is the disadvantage that these ray paths may end up reflecting water conditions that can vary significantly in the vertical. In the first case we presented, our double-surface bounce acoustic arrival time data and the calculated Kalman gain $\mathbf{K}$ results in a bias in the model predictions (Fig. 9) even though it is limiting the range of model solutions for water temperature. Work needs to be pursued to apply the modifications determined by the analysis fields to minimize the development of such biases. In our second test case (Fig. 11), we used knowledge of a model bias to limit the vertical extent of the assimilation process and, as a result, produce better model predictions.

In addition, we need to better understand the impacts of not discerning the exact path of an acoustic ray. There will always be inaccuracies in the latitudes, longitudes, and depths of a source and receiver as well as the bathymetry between the two. This leads to errors in the reference travel time t_R and the ΔL's (distances a ray travels through various model grid cells), both determined from the results of the acoustic propagation modeling. Bathymetric survey technology typically results in errors in depths of the order of meters. And errors in source, receiver, and bottom-bounce depths may or may not be cumulative. However, the latitudes and longitudes of hydrophones at depth (50+ m) obtained from a ship rolling on the open ocean are likely a greater source of errors for t_R and the ΔL's. It would not be unreasonable to expect such errors to be as large as tens of meters. Perhaps having multiple paths over numerous transects may mitigate such errors, but this has yet to be determined.

[1] W. Munk, P. Worcester, and C. Wunsch, *Ocean Acoustic Tomography* (Cambridge U.P., New York, 1995).

[2] B. Cornuelle, "Ocean acoustic tomography: Integral data and ocean models," in *Modern Approaches to Data Assimilation in Ocean Modeling*, edited by P. Malanotte-Rizzoli (Elsevier Science, Amsterdam, 1996).

[3] B. Cornuelle, W. Munk, and P. Worcetser, "Ocean acoustic tomography from ships," J. Geophys. Res. **94**, 6232–6250 (1989).

[4] C. G. Walter, "Data Assimilation for Ocean Acoustic Tomography," Ph.D. thesis, Applied Physics Lab., Univ. of Washington, 1999.

[5] S. E. Cohn, A. da Silva, Jing Guo, M. Sienkiewicz, and D. Lamich, "Assessing the effects of data selection with the DAO Physical-space Statistical Analysis System," Mon. Weather Rev. **126**(11), 2913–2926 (1998).

[6] A. F. Blumberg and G. L. Mellor, "A description of a three-dimensional coastal ocean circulation model," in *Three Dimensional Coastal Models, Coastal and Estuarine Sciences, 4*, edited by N. S. Heaps, Amer. Geophys. Union Geophysical Monograph Board (1987), pp. 1–16.

[7] V. Casulli and R. T. Cheng, "Semi-implicit finite difference methods for three-dimensional shallow water flow," Int. J. Numer. Methods Fluids **15**, 629–648 (1992).

[8] J. K. Lewis, Y. L. Hsu, and A. F. Blumberg, "Boundary forcing and a dual-mode calculation scheme for coastal tidal models using step-wise bathymetry," in *Estuarine and Coastal Modeling III: Proceedings of the 3rd International Conference*, edited by M. Spaulding *et al.* (ASCE, New York, 1994), pp. 422–431.

[9] W. H. F. Smith and D. T. Sandwell, "Global sea floor topography from satellite altimetry and ship depth soundings," Science **277**, 1956–1962 (1997).

[10] J. K. Lewis, I. Shulman, and A. F. Blumberg, "Assimilation of Doppler radar current data into ocean circulation models," Cont. Shelf Res. **18**, 541–559 (1998).

[11] G. D. Egbert, "Tidal data inversion: interpolation and inference," Prog. Oceanogr. **40**, 53–80 (1997).

[12] N. Booij, R. C. Ris, and L. H. Holthuijsen, "A third-generation wave model for coastal regions, Part 1, model description and validation," J. Geophys. Res. **104**(C4), 7649–7666 (1999).

[13] I. R. Young, *Wind Generated Ocean Waves*, edited by R. Bhattacharyya and M. E. McCormick, Ocean Engineering Series (Elsevier, Amsterdam, 1999).

[14] L. H. Kantha and C. A. Paulson, *Numerical Models of Oceans and Oce-*

anic Processes (Academic, New York, 2000).

[15] J. K. Lewis, "A three-dimensional ocean circulation model with wave effects," in *Estuarine and Coastal Modeling V*, edited by M. Spaulding and A. F. Blumberg (ASCE, New York, 1998), pp. 584–600.

[16] I. Shulman, C.-R. Wu, J. K. Lewis, J. D. Paduan, L. K. Rosenfeld, J. C. Kindle, S. R. Ramp, and C. A. Collins, "High resolution modeling and data assimilation in the Monterey Bay area," Cont. Shelf Res. **22**, 1129–1151 (2002).

[17] M. B. Porter and H. P. Bucker, "Gaussian beam ray tracing for computing ocean acoustic field," J. Acoust. Soc. Am. **82**, 1349–1359 (1987).

[18] M. B. Porter, P. Hursky, M. Siderius, M. Badiey, J. Caruthers, W. S. Hodgkiss, K. Raghukumar, D. Rouseff, W. Fox, C. de Moustier, B. Calder, B. J. Kraft, K. McDonald, P. Stein, J. K. Lewis, and S. Rajan, "The Kauai Experiment," in *High Frequency Ocean Acoustics*, edited by M. Porter, M. Siderius, and W. A. Kuperman, AIP Conf. Proc. (AIP, New York, 2004).